Thin-film micro-coil detectors: Application in MR-thermometry

Evdokia M. Kardoulaki [a],[*], Richard R.A. Syms [a], Ian R. Young [a], Marc Rea [b],
Wladyslaw M.W. Gedroyc [b]

[a] Optical and Semiconductor Devices Group, EEE Department, Imperial College London, Exhibition Road, London SW7 2AZ, UK
[b] Department of Radiology, Imperial College NHS Trust, Praed Street, Paddington, London W2 1NY, UK

ABSTRACT

Thin-film micro-coils are integrated with commercially available ablation catheters, for MR-thermometry during laser interstitial thermal therapies (LITTs). The coils are formed on a flexible polyimide substrate and consist of a two-turn electroplated copper inductor and integrated parallel plate capacitors for tuning and matching. Their performance was assessed during Nd:YAG laser ablations in a static phantom study carried out in a 3 T clinical scanner. Further moving phantom studies were performed to calculate errors due to motion. The temperature accuracy is improved by 1.5–10 times in a radius matching the dimensions of the lesions typically treated. Resolution of 1 mm can be maintained during motion by using short acquisition time sequences while the SNR remains sufficient for accurate MR-thermometry. The temperature error on a moving un-heated phantom under respiratory gating does not exceed 1 °C. This demonstration suggests a possible improvement of the overall control of MR-guided LITTs by local temperature monitoring.

1. Introduction

Micro-coils have received considerable attention from the magnetic resonance imaging (MRI) and spectroscopy communities, for biosensing, tracking of interventional devices, intravascular and internal organ imaging and MR-guided thermal therapies [1–8]. The increase in the signal-to-noise ratio (SNR) resulting from close coupling to the signal source, compared to volume and surface coils [9,10], makes micro-coils useful for fast, high resolution imaging, when a small field-of-view (FOV) can be tolerated.

Lack of repeatability and the effort required for matching and tuning using discrete components have limited clinical use. In recent years, micro and nano-fabrication techniques and the use of flexible substrates have opened up new design avenues [4,5,11–16], allowing the batch fabrication of disposable coils with repeatable coil parameters. Additionally, intense research effort has been invested in the safety of micro-coil-based catheters and many designs for improved patient safety have been reported [17]. We have recently presented thin-film detectors with mechanically tunable integrated capacitors [18], with potential application in the early diagnosis and staging of biliary carcinoma [19].

Here we explore a different application for thin-film micro-coils: improvement in the control of MR-guided laser interstitial thermal therapies (LITTs). Such minimally invasive therapies are increasingly used to destroy lesions in the liver and efforts are being made to improve their efficacy [20]. A key aim is to improve temperature accuracy during MR-thermometry [21]. High SNR is critical to accurate, real-time temperature monitoring, and can allow precise calibration of the MR thermal coefficients and quantification and exclusion of non-temperature related effects. Moreover, it can ensure that the impact of motion artefacts is minimised, by allowing faster sequences that still give useful SNR.

To date, only a few systems combining ablation devices with internal coils [8,22,23] have been proposed. None offers a disposable solution and no system has been reported for use during MR-guided LITTs, even though this is a well-established procedure for the treatment of small (<20 mm diameter), inoperable lesions. The paper is organised as follows: Section 2 describes the design, fabrication, and electrical performance of thin-film micro-coil detectors and details their integration with commercially available laser applicators. Section 3 describes the experimental set-up and phantoms used to assess their performance. Section 4 presents a comparison between the performance of the micro-coil system and an external array coil. Finally, discussions and conclusions are presented in Section 5.

2. Thin-film micro-coil detectors

In this Section, we describe the integration of a micro-coil with an ablation catheter. We outline the resonator design, the

* Corresponding author. Tel.: +44 (0) 207 594 6203.
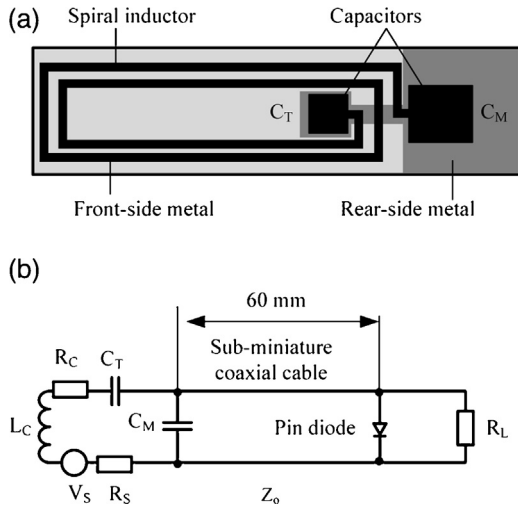*E-mail address:* ek03@ic.ac.uk (E.M. Kardoulaki).

Fig. 1. (a) Plan view of the thin-film micro-coil detector, (b) electrical equivalent circuit.

fabrication procedure and describe a method for identifying component values for matching and tuning at 127.6 MHz. Electrical performance is assessed using a network analyser (E5061A, Agilent Technologies).

2.1. Design and principle of operation

The micro-coil receiver is shown in Fig. 1a. It consists of a copper-clad Kapton thin film, patterned to form a two-turn spiral inductor with a pair of integrated capacitors C_T and C_M for tuning and matching. The inductor is connected to the two capacitors, each of which uses the substrate as an interlayer dielectric. The front side pattern consists of a spiral linked to two plates, while the rear side pattern consists of a pair of plates linked directly together. This layout places C_M outside the coil, allowing direct connection to a coaxial cable.

The layout can be fabricated from patterned conductors since no air-bridge is needed to exit the spiral. Double-sided processing is required but front-to-back alignment is not critical since capacitor plates need only overlap. Coils were designed with the following parameters: conductor width 150 μm, conductor separation 100 μm, coil length 60 mm, and coil width 4.5 mm. The last value was chosen to place the long conductors approximately on the diameter of the ablation catheter.

Fig. 1b illustrates the electrical equivalent. A shunt matching circuit has been preferred to avoid vias. For maximum power transfer, the signal induced by the external nuclear dipoles should be matched to a real load R_L at angular frequency ω_S using the capacitors C_M and C_T. The complex impedance of the parallel combination of R_L and C_M is $(1/j\omega \cdot C_M)\{1/(1 + 1/j\omega \cdot C_M R_L)\}$. If $\omega \cdot C_M R_L \gg 1$, this result may be approximated as $R_L' = 1/j\omega \cdot C_M + 1/(\omega^2 \cdot C_M{}^2 R_L)$. Matching requires a C_M such that $R_L' = R_C$ at the signal frequency:

$$C_M = 1/\{\omega_S \sqrt{(R_C R_L)}\} \tag{1}$$

Tuning involves choosing C_T so that the circuit is resonant at ω_S, which requires that the effective capacitance C_{eff} satisfies Eq. (2) with C_T positive, which in turn requires $\omega_S L_C > \sqrt{(R_C R_L)}$. C_M and C_T can be found by iteration after R_C, L_C have been determined. Both R_C and L_C can vary considerably without a well-controlled fabrication process.

$$1/C_{eff} = 1/C_M + 1/C_T = \omega_S^2 L_C \tag{2}$$
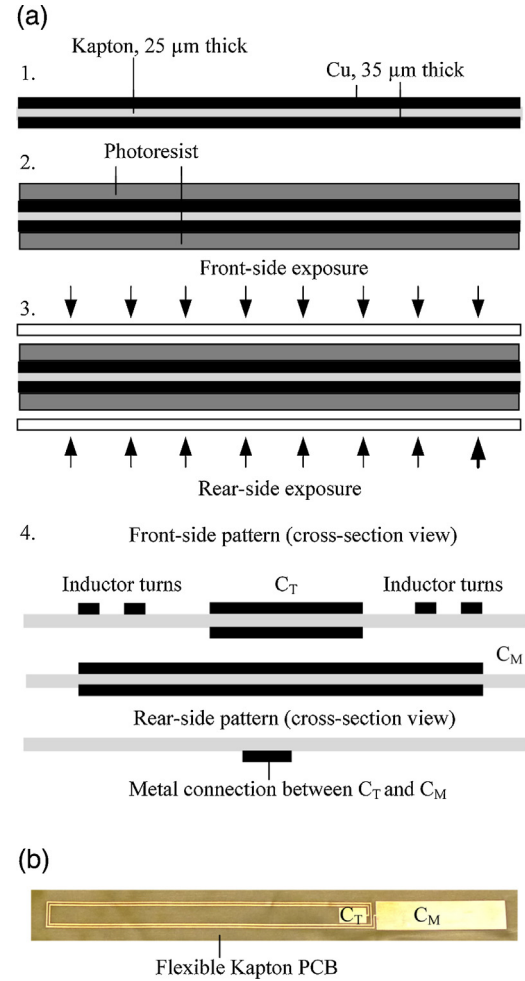

Fig. 2. (a) Process flow for detector fabrication, (b) batch-fabricated micro-coil with integrated tuning (C_T) and matching (C_M) capacitors.

2.2. Fabrication

Prototype devices were developed for 3.0 T ^{1}H MRI. Batch fabrication was carried out by the UK company Clarydon (Willenhall, West Midlands). The starting material is a 25 μm thick polyimide (Kapton®, HN, DuPont High Performance Films) carrying a 35 μm thick layer of Cu on either side. Patterning was carried out using double-sided exposure to a pair of photomasks formed from Mylar-coated silver halide on a 175 μm thick polyester backing. Masks were fabricated from a Gerber file.

The fabrication process is illustrated in Fig. 2a. Each side of the printed circuit board (PCB) (1) is coated with a 175 μm thick layer of laminated photoresist (2). The sensitised PCB is then sandwiched between the two photomasks on a glass backing using a set of pins passing through mating holes in each component for alignment. Textured Mylar spacers are used to assist evacuation. Each side of the PCB is exposed with an UV lamp (3). Resist development and metal etching are carried out with the PCB horizontal, using a leader board to allow dragging through a spray developer and etcher. The resist is then stripped (4). A fabricated device is shown in Fig. 2b.

L_C and R_C were determined in an iterative process to choose the correct areas for C_M and C_T prior to the design of the photomasks. A set of inductors was first fabricated without capacitors (Batch 1), but with bond-pads to allow addition of a wire-bond air-bridge and surface-mount capacitors, which were adjusted to match to 50 Ω and tune to 127.6 MHz. A second set of devices was then fabricated with integrated capacitors (Batch 2), using areas for

C_M and C_T estimated from Batch 1. The capacitors were then trimmed to match and tune with a fixed tissue loading.

2.3. Matching and tuning for use in a 3T scanner

Final matching and tuning was carried out with the coil flat and a sub-miniature co-axial cable connected across C_M. Matching was ensured by minimising S_{11} at 127.6 MHz. Ignoring intrinsic capacitance, the coil resistance R_C was estimated as 3.2 Ω, implying a value of $C_M = 100$ pF and hence a matching capacitor length of 1.33 cm, given a matching capacitor width of 5 mm and a Kapton thickness of 25 μm. The matching capacitor was then trimmed using a scalpel. The value of C_T and the required tuning capacitor length were then estimated from Eq. (2) and C_T was trimmed to match the calculated values.

An unloaded Q factor of 60 was measured implying good performance from the integrated capacitors and a value of $S_{11} = -35$ dB suggesting good matching. Tissue loading was investigated by inserting a detector loosely attached to an ablation catheter by a heat-shrink sleeve into an agar gel phantom with a salt content chosen to mimic the conductivity of liver (see Section 3.2). Loading caused a reduction in the resonant frequency of > 12 MHz, mainly due to an increase in self-capacitance caused by the change in dielectric surround, and a reduction in Q-factor due to the tissue conductivity. A loaded Q factor of 30 was measured, again indicating good matching.

2.4. Integration with the ablation catheter

A micro-coil was tuned and matched for 3T following the procedure described in Section 2.3. The detector was deliberately tuned to a higher resonant frequency, in order to operate correctly after tissue loading. A sub-miniature coaxial cable with a non-magnetic pin diode (MA4P7464F-1072, MACOM) connected in shunt at 60 mm from C_M enabled active detuning as shown in Fig. 1b. The length of the coaxial cable was estimated from a Matlab™ model which determined the optimal length for maximum coupling of the two resonant circuits formed by the micro-coil inductor, with the coaxial cable acting as an inductor of inductance $Z_0 \tan(\beta l)$, with $\beta = 2\pi f/\nu$ ($\nu = 2.25 \cdot 10^8$ m/s), when the pin diode is ON, during RF excitation.

The completed micro-coil was combined with a Somatex (Power-Laser Applicator Set, SOMATEX, Teltow, Germany) water-cooled laser applicator, as shown in Fig. 3a. An inner PTFE tube (OD 3.9 mm, ID 3.4 mm) was slid over the applicator and the micro-coil was wrapped around it. An outer heat shrink sleeve (ID 4.1 mm, OD 4.8 mm) provided sealing and secured the coil in position.

The electrical characteristics of the assembled probe are shown in Fig. 3b and confirm adequate decoupling and patient safety since heating due to imperfect decoupling would not be a concern. Furthermore, heating due to excitation of standing waves in the conductors by the E-field of the transmitter can be assumed to be minimal, since the coaxial length is much smaller than the length required for resonance of an immersed line [24]. The control signal for decoupling during RF excitation was generally provided by the scanner. However, during experiments with an additional array coil, the micro-coil was decoupled using a DC signal derived from a 10 V battery with an 80 Ω limiting series resistor.

3. Magnetic resonance imaging experiments

In this Section we discuss the methods used to evaluate the performance of the micro-coils for MRI and proton resonance frequency (PRF) MR-thermometry. The measurements are summarised in Table 1 and Table 2 provides the MR-parameters used for each measurement.

3.1. Imaging set-up and laser system

MR imaging was carried out in a 3T GE Signa Excite scanner (GE Healthcare, Milwaukee, WI, USA). The image quality, SNR and PRF MR-thermometry accuracy were compared with the corresponding performance of an 8-channel array coil (GE MRI 3T Split III Total SENSE Cardiac Coil) used for MR-thermometry at St. Mary's Hospital. A Nd:YAG laser (MY 30, Marting Medizin-Technik, Tuttlingen, Germany) with a wavelength of 1064 nm and 25 W output power was used during ablations. The internal circulation cooling system of the applicator was maintained by a continuous flow of 0.9% NaCl at a rate of 60 ml/min. The laser light was delivered through a 12 m length of fibre with a 400 μm diameter core and a 20 mm diffuser active tip (Surgical Laser Technology).

3.2. Phantom preparation and characterisation

Agar gel phantoms with time constants of T_1 of 800 ms and T_2 of 50 ms, mimicking those of liver tissue [25], were used in this study. For the ablation, a gel doped with 8% India ink was used. Its absorption coefficient was determined by transmission spectroscopy as 0.12 mm^{-1} at 1064 nm wavelength. In all experiments, body loading was provided either by casting the ablation phantom in the gel or by means of standard cuboid phantoms. For a quantity of 700 ml gel, 31.5 g agar was mixed with 58 ml n-propanol and 642 ml of a salt solution containing 3.37 g/L NiCl$_2$·6H$_2$O and 2.4 g/L NaCl.

3.3. Experimental arrangements

3.3.1. Static phantom

The arrangement for the static comparison of SNR and temperature accuracy provided by the two coils is shown in Fig. 4a. The details of the axial thermometry slices are illustrated on the schematic of Fig. 4b. Ink-doped agar gel was moulded in a cylindrical structure constructed from Plexiglass slices (9.5 mm thick) and supported in a further container filled with 1.4 l of tissue-mimicking agar gel (0% ink) to emulate body loading. The probe was cast horizontally.

Two fibre optic sensors based on fluorescent lifetime[1] (Type 790, Luxtron, Santa Clara, CA, USA), with accuracy ± 0.1 °C, provided references against the MR-inferred temperatures at $d = 5$ mm (L_1) and $d = 10$ mm (L_2) to the probe in each monitored slice. For the comparison, the set-up of Fig. 4a was positioned between the anterior and posterior cardiac array coil elements at a distance of 70 mm to the probe axis from either side.

3.3.2. Moving phantom

The periodic motion of liver due to breathing was simulated using a hydraulically driven suspended table. The motion simulator consists of a movable stage, supported on multiple balanced flexures, machined from a piece of Delrin (Polyoxymethylene). The motion is controlled by a hydraulic engine powered by a unipolar stepper motor driver and equipped with flip-flop logic to enable periodic motor reversal between limits set by a pair of microswitches. A pair of hydraulic rams linked with the engine, drive the suspended table by means of 10 m of water-filled flexible line, running between the control and the magnet rooms. The set-up is shown in Fig. 4c.

---

[1] We refer to the Luxtron fibre optic sensors based on fluorescent lifetime with their trade-name "fluoro-optic" or "Luxtron" sensors in the rest of the manuscript.
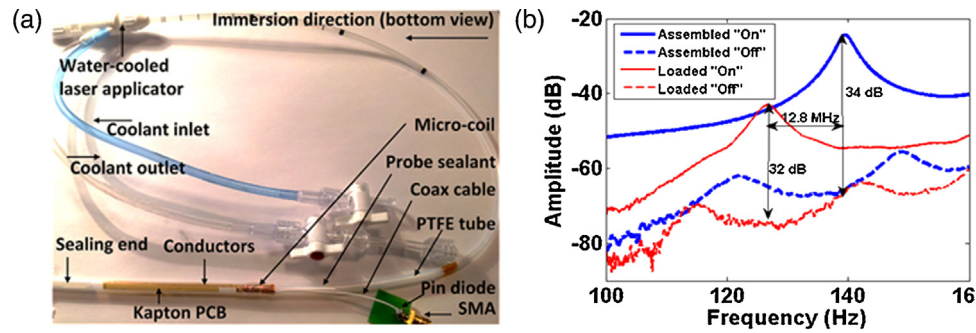
Fig. 3. (a) Modified laser applicator with integrated micro-coil receiver and (b) S-parameters of the micro-coil tuned and matched for use in a 3T scanner; both unloaded and loaded with 700 ml tissue mimicking agar gel.

Table 1
Summary of the measurements described in Section 3.

	Measurement type	Results	Phantom	MR sequence	MR-parameters
1	Image quality	Fig. 5a and b	Static (Fig. 4a)	2D Spin echo	Sequence 1
2	SNR comparison	Fig. 5d–f	Static (Fig. 4a)	2D Spin echo	Sequence 2
3	SNR and image quality comparison	Fig. 6a and b	Static/Moving (Fig. 4d)	2D Gradient echo	Sequence 3
4	SNR and TSD comparison	Fig. 7a and b	Static (Fig. 4a)	2D Gradient echo	Sequence 4
5	PRF MR-thermometry comparison	Figs. 7c–f and 8	Static (Fig. 4a)	2D Gradient echo	Sequence 4
6	Pixel cross-correlation, temporal phase stability and TSD	Fig. 9	Static/Moving (Fig. 4d)	2D Gradient echo	Sequence 3

Table 2
MR-parameters used for each measurement described in Table 1.

	Sequence 1 Measurement 1	Sequence 2 Measurement 2	Sequence 3 Measurements 3 and 6	Sequence 4 Measurements 4 and 5
TR	400 ms	400 ms	7.67 ms	7.976 ms
TE	13 ms	13 ms	3.85 ms	3.872 ms
FA	90°	90°	20°	20°
Pixel BW	122.109 Hz	122.109 Hz	244.141 Hz	244.141 Hz
Slice thickness	8 mm	8 mm	3 mm	10 mm
Slice spacing	10 mm	10 mm	3 mm	10 mm
FOV	200 mm × 200 mm	120 mm × 120 mm	160 mm × 80 mm	120 mm × 120 mm
Matrix	192 × 192	192 × 192	256 × 64	256 × 224
Orientation	Sagittal	Axial	Axial/Sagittal	Axial
Voxel size	$0.78 \times 0.78 \times 8$ mm^3	$0.46 \times 0.46 \times 8$ mm^3	$0.625 \times 0.625 \times 3$ mm^3	$0.46 \times 0.46 \times 10$ mm^3
Acquisition time	1.28 min	1.28 min	0.49 s	1.78 s
Temporal resolution[a]	–	–	4.4 s	6 s
Total Acquisition time	15.36 min	15.36 min	44 s	62.5 min (micro-coil)50 min (array coil)

[a] Temporal resolution refers to the time interval between consecutive image acquisitions of a given image slice.

For gating, the operation of a respiratory bellows was replicated by sensing the pressure changes of air inside a PTFE pipe, connected to the MR scanner at one end and to a further syringe, driven by the movement of the table, at the other. The movement is in the superior-inferior direction and the travel distance was adjusted to ±14 mm. A full cycle repeated every 4.4 s, corresponding to 14 breaths per minute. The ablation phantom was attached to the moving table and two 10 kg cuboid phantoms (15 cm × 15 cm × 38 cm), supported above the table at either side, provided body loading as shown in Fig. 4d. Three phantoms with features of 1 mm, 2 mm and 3 mm, immersed at 5 mm above the probe, were used to assess the impact of motion artefacts on resolution.

3.4. Data processing

3.4.1. SNR

Spin echo and gradient echo sequences were used for the assessment of the image quality and the static SNR comparison (Table 1, measurements 1, 2 and 4). The sequence parameters are detailed in Table 2. The sensitivity was evaluated by constructing pixel-by-pixel SNR maps of corresponding slices and the radial SNR profiles

were evaluated along a horizontal line passing through the phantom diameter.

The pixel SNR was defined according to Eq. (3), where the signal (S) refers to the signal intensity of each pixel and the noise to the standard deviation (SD) in an N × M region-of-interest (ROI) in the background of the same image slice, in a region with no signal sources. The scaling factor of 0.66 was used to account for the Rayleigh noise distribution [26]. For the calculation of the SNR in a chosen ROI, the signal (S) in Eq. (3) was defined as the mean signal in the ROI.

$$SNR = 0.66 * S/SD \qquad (3)$$

The comparison was repeated under simulated periodic motion, with a more realistic loading emulated by the cuboid phantoms shown in Fig. 4d (Table 1, measurement 3). Large FOV axial and sagittal slices were acquired with a 2D gradient echo sequence with acquisition time of 0.49 s. The rest of the details of the sequence are provided in Table 2. The phase encoding direction was deliberately chosen not to lie in the direction of motion.

Ten temporal frames were acquired both with and without respiratory gating (Table 1, measurement 3). The mean SNR over all frames was calculated in a chosen ROI in the images of the stationary phantom and the results were compared with the
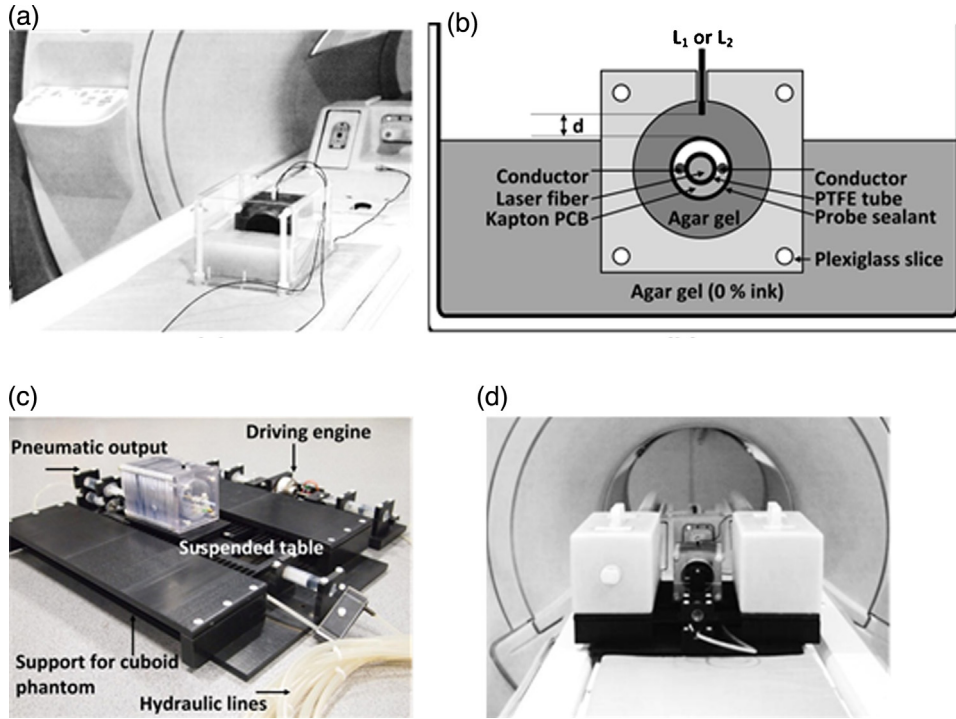
Fig. 4. (a) Arrangement for the static SNR and MR-thermometry comparison studies, (b) schematic of an axial thermometry slice of the set up in (a), showing the position of the fluoro-optic sensors relative to the micro-coil probe and the details of the micro-coil assembly on the laser applicator, (c) hydraulic simulator of liver motion due to breathing and (d) complete arrangement for the assessment of motion artefacts.

corresponding SNR values from slices of the moving phantom. For completeness, both the SNR definition of Eq. (3), and the dual acquisition SNR definition described in Eq. (4) were used. In the latter case, the noise is defined as the SD in an $N \times M$ ROI in the phantom region of the difference image of two consecutively acquired frames of a given slice.

$$\text{SNR} = \sqrt{2} \times S_1 / SD_{1-2} \qquad (4)$$

3.4.2. Reference-based PRF MR-thermometry

The PRF MR-thermometry performance of the micro-coil (Table 1, measurement 5) was assessed by simultaneously monitoring the spatiotemporal thermal profile of two axial slices of the static phantom (see Fig. 4b) using a 2D gradient-echo thermometry sequence with the parameter details indicated in Table 2. The results were compared with those obtained in a subsequent ablation of the same phantom using the array coil this time.

Data analysis was performed offline in Matlab™ by post-processing the phase images from the two slices that were acquired during ablations. The position of the fluoro-optic probes was registered on high-resolution images of the thermometry slices and the average pixel values, within a 2×2 ROI under each Luxtron sensor, were used to estimate the phase differences ($\Delta\varphi$) from corresponding baseline images acquired before turning the laser on in each case. The phase differences were then converted into temperature differences according to Eq. (5) [21].

$$T_{(n)} = \Delta\varphi / (a \cdot \gamma \cdot B_0 \cdot TE \cdot 360) + T_{\text{ref}} \qquad (5)$$

Here T_{ref} is the temperature recorded with the Luxtron sensors at the beginning of the experiment (baseline), a is the PRF shift coefficient (ppm/°C), $\gamma/360°$ is the gyromagnetic ratio (45. 2 MHz/T), B_0 is the static magnetic field (3T), TE is the echo time (3.872 ms). The thermal coefficient a was determined from the linear fit of the phase differences (in the ROI corresponding to L_1), plotted against temperature differences recorded with L_1. Two non-heated ROIs

(10×30 pixels) were used to correct for non-temperature related phase changes.

The temperature error of the PRF MR-thermometry for either coil was assessed by plotting the deviations of the MR-inferred temperatures from the temperatures recorded with the Luxtron sensors in each slice. The noise in the temperature measurement was estimated by means of the temperature standard deviation (TSD) expressed in Eq. (6) [27,28] and using an SNR defined according to Eq. (3).

$$\text{TSD} = 0.66 / (\text{SNR} \cdot \alpha \cdot \gamma \cdot TE \cdot B_O) \qquad (6)$$

3.4.3. Temporal phase stability

Without motion correction, the reference-based PRF MR-thermometry method would generate temperature errors due to inter-scan motion artefacts in mobile organs such as liver [21]. One source of error is the misalignment of the nth image during ablation from the baseline used for the subtraction, while another is the change in local susceptibility, due to changes in the shape of the liver.

The impact of motion on the micro-coil reference-based PRF MR-thermometry was assessed using the set-up of Fig. 4d (Table 1, measurement 6). Ablation was deliberately not carried out, so that the temperature of the phantom remained unchanged. This allowed the estimation of the errors caused due to non-temperature related phase changes. Ten temporal frames of axial and sagittal slices were acquired under respiratory gating, using a similar MR-thermometry gradient echo sequence to that used during the ablations of the static phantom (Table 1, measurement 5). The sequence parameters are summarised in Table 2.

Prior to this, the degree of misalignment between the baseline image (i.e. the 1st frame) and each of the other acquired images was determined on magnitude images by calculating the pixel-by-pixel cross-correlation described by Eq. (7), where the baseline image is annotated by X while Y_n is the nth image frame and k the voxel index. Y_{mean}, X_{mean} represent the signal average of each image. For
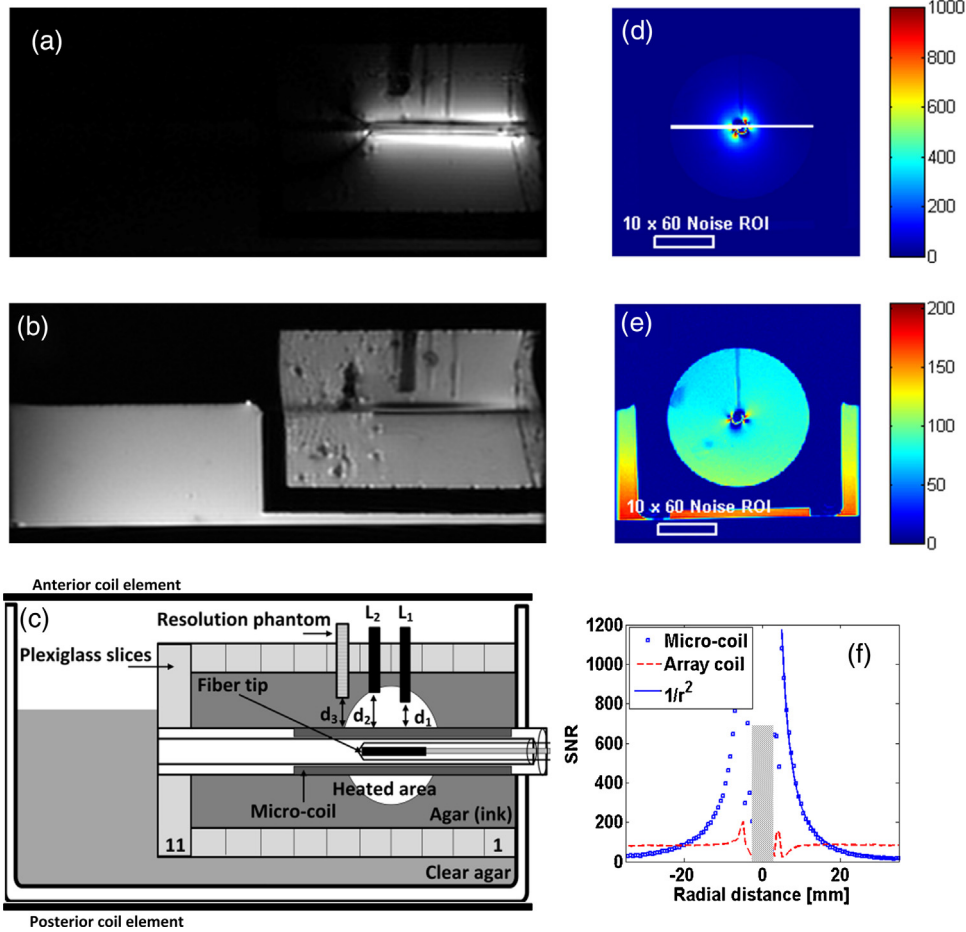
Fig. 5. Large FOV sagittal slice images of the static phantom illustrating the two fluoro-optic sensors (L_1 at 5 mm and L_2 at 10 mm to the probe axis): (a) micro-coil, (b) array coil and (c) corresponding schematic; SNR maps of axial slice images showing L_1: (d) micro-coil, (e) array coil; (f) radial SNR profiles along the line in d.

$P_{XY} > 0.95$, misalignment was excluded as a cause for the calculated phase difference on a given voxel [26].

$$P_{XY} = \frac{[(X_k - X_{\text{mean}})(Y_{n,k} - Y_{\text{mean}})]}{\sqrt{[(X_k - X_{\text{mean}})^2 (Y_k - Y_{n,\text{mean}})^2]}} \tag{7}$$

The impact of residual motion artefacts on the temporal phase stability was then determined by evaluating the mean phase difference and deviation from the baseline temperature of 20 °C, over the 10 acquired frames, for each of the pixels in a line along the direction of motion, in a sagittal slice of the phantom. The results were compared with the static case, to assess the contribution of motion to temperature error. The pixel-by-pixel temperature standard deviation (TSD) maps were also evaluated based on Eq. (6), using an SNR defined according to Eq. (3). The tests were repeated using the array coil for comparison.

4. Results and discussion

4.1. Image quality and SNR performance

Fig. 5a and b shows large FOV sagittal images obtained with the micro-coil and the array coil, respectively. A corresponding schematic is shown in Fig. 5c. The micro-coil image is free from artefacts and the fluoro-optic sensors can be clearly seen. The non-uniform sensitivity and small FOV of the micro-coil are confirmed. The image contrast is lost in the left hand side (LHS). Although it is

possible that an air-material boundary exists, the images obtained do not suggest any strong susceptibility artefacts due to that.

Referring to the array coil image, there are no susceptibility artefacts due to the micro-coil and good decoupling is confirmed. The ink-doped gel has lower signal intensity compared to the surrounding gel together with some bubbles. The bubbles were transferred from the top of the beaker containing the prepared gel to the bottom of the phantom which was mounted vertically during transfer and casting. This explains the difference in the uniformity of the gel observed in Fig. 5b.

SNR maps for corresponding micro-coil and array coil small FOV axial slices featuring sensor L_1 are shown in Fig. 5d and e respectively. Referring to Fig. 5e, despite the expected uniform SNR in the array coil image, non-uniformity appears. This has been observed in many previous experiments we have conducted using the specific coil (best locally available). We have established that the uniformity of the array coil is in fact a function of the load and the separation between its anterior and posterior coil elements. In this experiment here, the separation was 140 mm, which may be below the average patient size for which the array is set up.

Symmetrical patterns of voids near the micro-coil conductors affect both images. Their origin is imperfect decoupling. They occur with all coils and all decoupling schemes, but are generally not noticed because of their short range. However, they will always be obvious when a local coil is completely immersed in a signal source. Such artefacts could be reduced by using adiabatic pulses and excitation as well as reception from the micro-coil. The latter could also improve coil-dependant, non-uniform phase variations, since
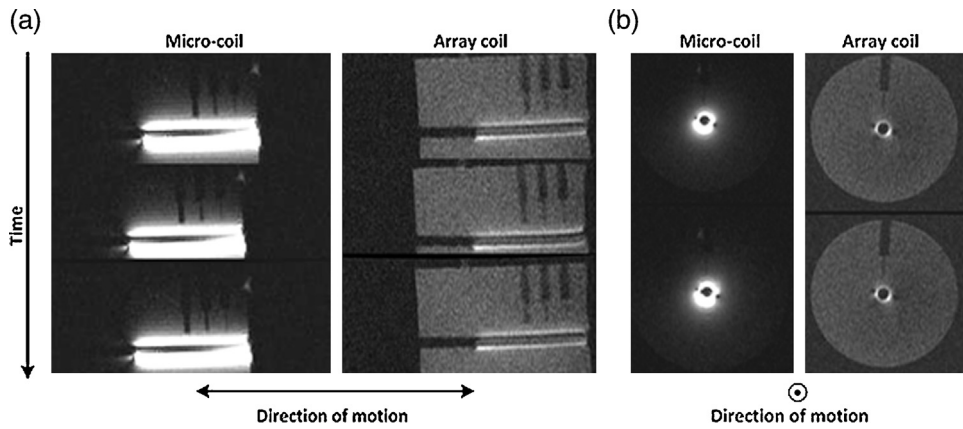
Fig. 6. (a) Large FOV sagittal slices of the moving phantom showing the 1, 2 and 3 mm features of the resolution phantoms and (b) large FOV axial slices (cropped), with respiratory gating in place, showing the resolution phantom with the 1 mm feature. All images have been acquired using a 2D FGRE sequence with 0.49 s acquisition time.
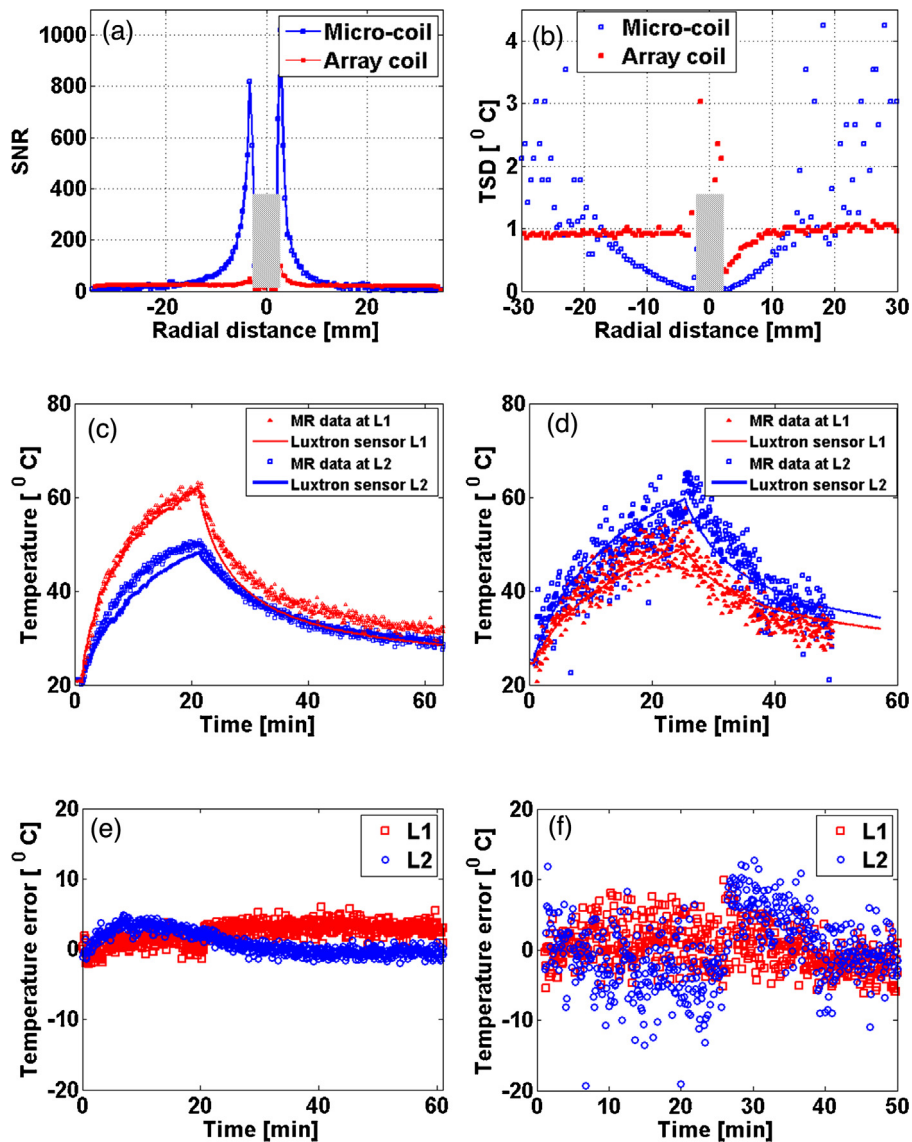

Fig. 7. (a) Radial SNR profile of the baseline image corresponding to L_1, (b) corresponding radial temperature standard deviation (TSD) (°C); comparison of MR-inferred transient temperatures with the fluoro-optic readings: (c) micro-coil and (d) array coil; temperature error, defined as the deviation of the MR-inferred temperatures from the Luxtron readings: (e) micro-coil and (f) array coil.
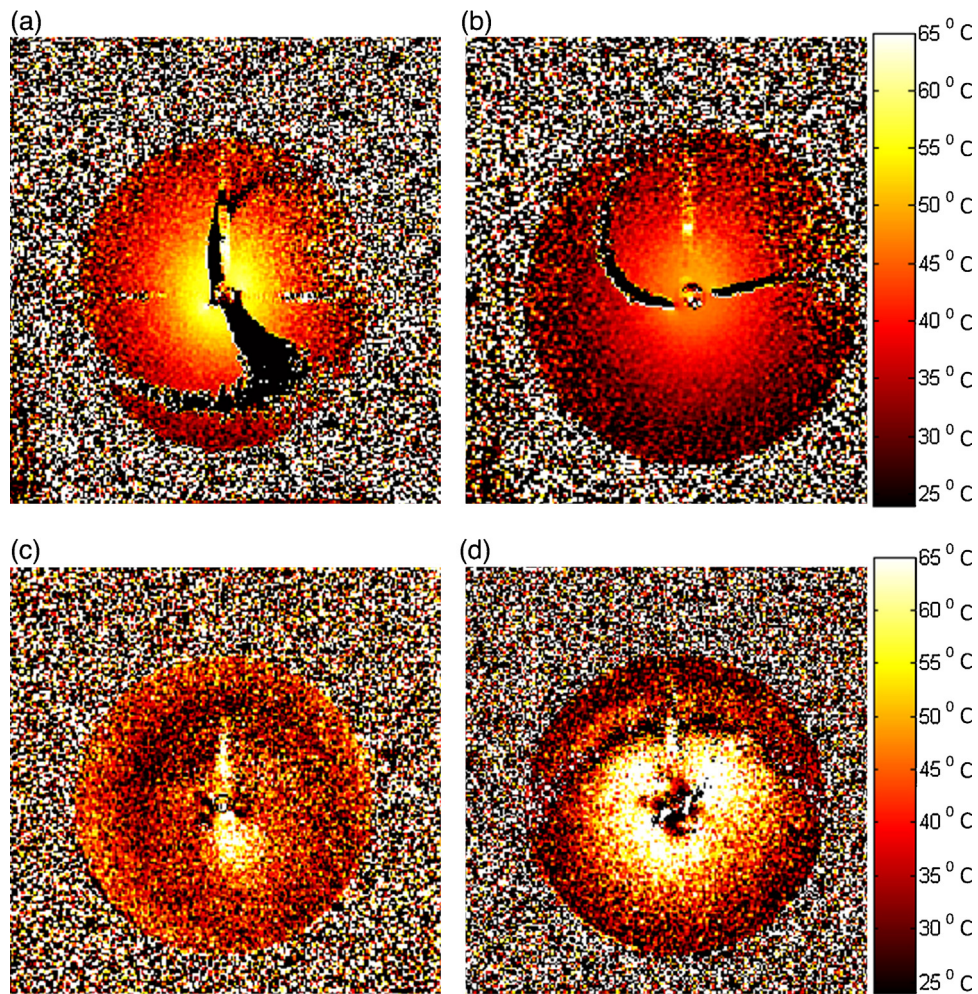
Fig. 8. Temperature maps corresponding to the time the laser was turned off in each ablation: (a) micro-coil, slice containing L_1, (b) micro-coil, slice containing L_2, (c) array coil, slice containing L_1 and (d) array coil, slice containing L_2.

the transmit and receive phase variations would then be expected to cancel [29]. Adiabatic pulses have not been investigated here and although they might have advantages they cannot improve the relative increase in SNR.

The radial SNR profiles are shown in Fig. 5f. In the case of the micro-coil, a $1/r^2$ curve has been fitted with good correlation ($R^2 = 0.99$). At 7.5 mm from the probe centre the SNR is equal to 647, while the respective value for the array coil is 86, implying a 7.5-fold improvement. At a 20 mm radius, the SNR values of the two coils become equal. The SD in the indicated ROI is equal to 8.6 in the micro-coil axial slice (Fig. 5d) while the corresponding value on the array coil slice (Fig. 5e) is equal to 10. Various sizes of ROI, at the same and different locations have been considered with negligible difference to the calculated SNR.

Three sagittal slices, of the moving phantom, are shown in Fig. 6a for both coils and two axial slices obtained with respiratory gating are shown in Fig. 6b. The 1 mm feature can be clearly seen in all micro-coil sagittal images. In contrast, this feature is blurred in the array coil images. The respiratory gating operated well since the slices from both coils appear stationary. This was also independently confirmed by calculating the pixel-by-pixel cross-correlation. For the array coil, the 1 mm feature can be seen more clearly in the axial slices.

The SNR was not affected from the motion (with and without respiratory gating) for none of the coils. At 5 mm to the probe on the micro-coil axial slices it is equal to 137 with the definition of the

Eq. (3). The mean SNR value, over all ten frames of a sagittal slice (in a 30 mm × 10 mm ROI centred at the probe below the resolution phantoms) is equal to 100. The corresponding array coil SNR value is less, by a factor of 8. The respective mean SNR values using Eq. (4) are 1.5 times higher for both coils. The SD for these measurements is 18 and 22 for the micro-coil and the array coil image slices respectively.

4.2. Reference-based PRF MR-thermometry accuracy without motion

Fig. 7a shows the radial SNR on the axial baseline images corresponding to L_1. The SNR of the array coil is almost constant and equal to 23. At 5 mm radius, the SNR of the micro-coil is 10 times higher and remains 1.5 times higher up to a 15 mm distance. The TSD using the SNR definition of Eq. (3) is less than 0.75 °C up to 20 mm and less than 4.5 °C up to 30 mm, as shown in Fig. 7b. In the micro-coil image slice used for these calculations, the SD is equal to 10 and the corresponding value for the array coil is equal to 14.

Worth noting is that in the SNR comparisons with either the spin-echo sequence (Table 1, measurement 2) or the gradient-echo sequence (Table 1, measurement 4), there is no significant difference between the noise values (SD) calculated in corresponding images acquired with either coil. This suggests that the signal enhancement offered by the micro-coil has more weight in the SNR improvement.
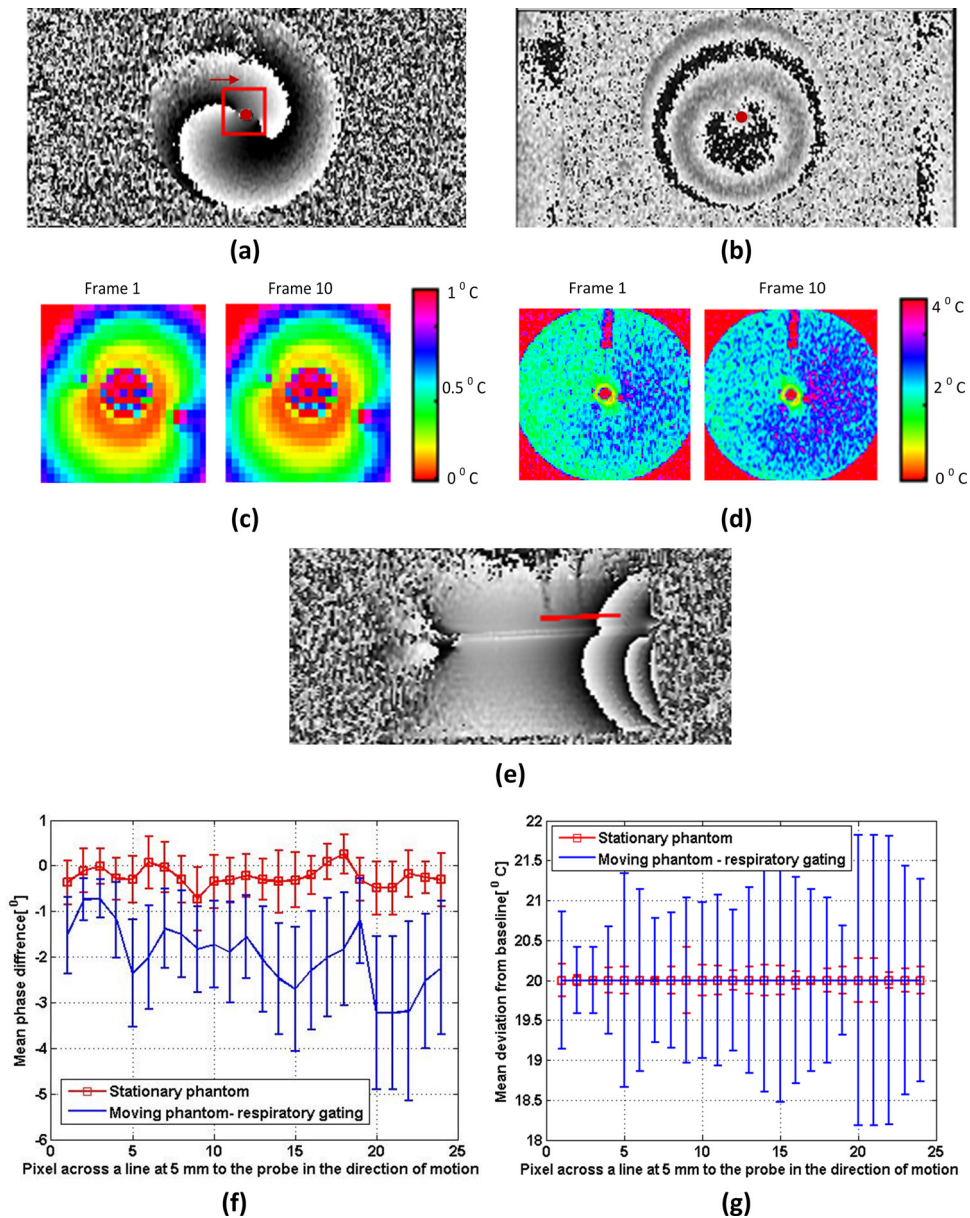
Fig. 9. Phase images of the 1st frame (in a series of 10) of corresponding axial slices of the moving phantom, with respiratory gating, showing the 1 mm feature: (a) micro-coil and (b) array coil; pixel-by-pixel temperature standard deviation (TSD) maps: (c) micro-coil in the 15 × 15 mm ROI indicated in (a) and (d) array coil covering the whole area of the cylindrical phantom; (e) Micro-coil sagittal phase image of the 1st frame; (f) Mean phase differences for each pixel along the line indicated in (e) and (g) mean deviation of the MR-inferred temperatures from the nominal baseline temperature of 20 °C.

Fig. 7c and d compares the MR-inferred temperatures obtained from each coil with the fluoro-optic sensor readings. We have estimated the PRF shift thermal coefficient as -0.01 ± 0.009 ppm/°C and the results of Fig. 7c–f are derived based on Eq. (5) and using this value. During the preparation of the set up for the array coil ablation, the applicator was accidentally displaced axially to the left by approximately 10 mm, leading to a similar shift of the heating zone and hence to the recording of lower temperatures by sensor L_1 and of higher temperatures by sensor L_2 compared to the micro-coil ablation, as seen in Fig. 7c and d. This was unfortunately not noticed until after processing the data.

There is also a small difference in the starting temperatures of the two ablations. The array coil ablation was necessarily initiated after the micro-coil ablation but before the gel had time to cool down to the exact same starting temperature due to restricted continuous scanner time. These minor experimental deficiencies do

not however alter the basic findings of the experiment, namely the high gain in the SNR and the respective improvement in the PRF MR-thermometry.

Referring to Fig. 7c and d, the temperature measurement in the micro-coil case is significantly less noisy locally. This is also confirmed by the plot of the radial TSD shown in Fig. 7b, which is a measure of the noise in the temperature measurement. For the micro-coil, there is a good correlation with the fluoro-optic readings. Despite correcting for phase changes unrelated to temperature, slight deviation from the fluoro-optic temperatures can be observed in Fig. 7c. This could be attributed to changes in susceptibility or electrical conductivity of the gel with temperature [21,29].

For example, thermal expansion, or changes in the susceptibility of air bubbles in the ablation phantom might have affected the measurements [30]. An alternative approach might be to exploit the

temperature insensitivity of the lipid protons and use fat reference phantoms in the un-heated region as a correction [31]. However, this technique might be challenging to implement in the liver. The deviations occur at different times for L_1 and L_2 because the temperatures are derived from two different slices and it is likely that non-temperature related phase changes occurred at different times in each slice.

For the array coil, due to the noisy data, it is difficult to notice the deviation from the Luxtron readings based on Fig. 7d. Those become obvious in Fig. 7e and f where the deviation of the MR-inferred temperatures in each case from the Luxtron readings have been plotted over the duration of each ablation. The maximum deviation from the Luxtron readings (or temperature error) is equal to 6 °C for the micro-coil while the corresponding value for the array coil is 20 °C. It is therefore clear that the high local sensitivity of the micro-coil can be exploited to detect non-temperature related phase changes and correct for them. This is not easy in the case of the array coil since the data is so noisy.

No effect on the readings of Fig. 7c and d was noticed due to the operation of the Nd:YAG laser [27]. We have also not noticed any flow-related artefacts due to the circulation of the cooling water in the applicator. Finally the melting point of the gel is 100 °C which was not reached during ablations even in the vicinity of the applicator as verified by the temperature maps shown in Fig. 8 for each slice and each ablation at the time the laser was turned off. Based on that, it is unlikely that convection has introduced temperature errors.

4.3. Temporal phase stability during motion

The 1st frame of the micro-coil axial phase image is illustrated in Fig. 9a, showing the 1 mm feature. A corresponding array coil image of significantly poorer quality is shown in Fig. 9b. Fig. 9c illustrates the micro-coil TSD maps corresponding to the 1st and last frame in the 15 mm × 15 mm ROI shown in red in Fig. 9a. The respective array coil TSD maps, covering the whole cross-section of the cylindrical phantom, are shown in Fig. 9d.

The TSD maps have been calculated using the SNR definition of Eq. (3). Little variation was observed across the 10 frames, especially for the micro-coil. Fig. 9e is a micro-coil sagittal phase image. It shows the three resolution phantoms and indicates the line of pixels (at 5 mm radius to the probe axis, with length equal to 15 mm) for which the mean phase differences and temperature errors, were evaluated across ten acquired temporal frames.

Fig. 9f shows the mean micro-coil phase difference for each of the pixels in the line. The error bars correspond to the standard deviation across the ten acquired frames. The mean MR-inferred temperature deviations, over all frames, from the nominal temperature of 20 °C are shown in Fig. 9f in the form of error bars.

Despite the good operation of the respiratory gating, residual motion artefacts lead to susceptibility changes that affect the calculated phase difference from the baseline and hence lead to temperature errors. The maximum temperature error does not however exceed 2 °C for any of the pixels in the line while for the stationary phantom the temperature error is as low as the calculated TSD. Finally, the mean TSD values across all frames are equal to 0.27 °C (in the ROI shown in Fig. 9c) and 3 °C (in the ROI shown in Fig. 9d) for each coil respectively, implying a 10-fold reduction in the noise of the temperature measurement.

Finally, in a ROI of 15 mm × 15 mm, the maximum temperature error is equal to 1 °C for the micro-coil while the respective value for the array coil is four times higher. Finally, the maximum micro-coil phase error across all frames and pixels in the line along the direction of motion is equal to 0.5° on the static phantom with a 2° standard deviation. The respective maximum phase error value in the moving phantom is six times higher.

5. Conclusion

We have designed and fabricated thin-film micro-coil resonators and demonstrated their integration with laser ablation catheters without modification to their clinical functionality. The system is designed for local MR-thermometry during Nd:YAG laser ablations performed in clinical 3T scanners. The micro-coils can be batch fabricated on flexible Kapton substrates, yielding disposable coils with well-defined, stable parameters, and the integrated capacitors lead to a compact solution while providing a simple approach to tuning and matching.

The improvement in the local PRF MR-thermometry has been demonstrated in a static gel phantom with liver-mimicking optical and MR-properties. The image quality, resolution and SNR were significantly better than corresponding results obtained from the best locally available array coil, while the temperature deviation from the Luxtron readings was also significantly less. This performance compares well with other studies using internal coils [8,22,23]. Although beyond the scope of this paper, further improvement could result from optimisation of the thermometry sequence [27] and the use of better correction methods for non-temperature related phase changes.

For an external surface coil to achieve similar performance, the scan time would have to increase prohibitively. The improved SNR was confirmed under two different body loading conditions, one of which mimicked the in vivo case, resulting in poor array coil image quality compared to the less realistic scenario.

Since motion of organs such as liver due to breathing can be a critical source of temperature errors in the reference-based PRF method [21] we assessed the robustness of the micro-coil under respiratory gating in a constant-temperature phantom. Good operation of respiratory gating was confirmed, for both coils. Despite the absence of image misalignment errors, residual local susceptibility variations led to temperature errors for both coils but significantly higher for the array coil case.

Remaining concerns prior to consideration for clinical use regard the coil orientation and the opto-thermal characterisation of the modified ablation catheter. In vivo studies employing animal models will be required to simulate a more realistic scenario, where effects such as non-periodic motion of the liver and load-dependent variations in the resonant frequency and Q-factor are taken into account. Variations of the resonant frequency and the Q-factor of the coil due to heterogeneity in the load conductivity would be problematic since the imaging performance might deviate from the optimal. It would therefore be important to fully characterise such variations using human tumour models.

The deterioration in SNR due to a probe orientation other than the optimal horizontal used here should also be examined, although the insertion angle of >80° required to cancel the expected 10-fold improvement in the SNR is highly unlikely in a clinical scenario. We have verified that patient safety or uneven heating of the lesion due to the presence of the Kapton film around the catheter are not a concern. More specifically, we have established that the absorption of the Kapton substrate at 1064 nm is less than 20%. However, further work in progress aims at the complete characterisation of the opto-thermal behaviour of the catheter.

Despite the need for further studies, the preliminary results presented here suggest the potential of micro-coils for improved PRF MR-thermometry. Besides this, they may assist the clinician in ensuring the correct ablation site, and in principle, allow MR-thermometry to be carried out without the use of the cumbersome

and restrictive external array coil, greatly improving access to the patient.

Acknowledgements

References

[1] S.S. Zalesskiy, E. Danieli, B. Blümich, et al., Miniaturization of NMR Systems: desktop spectrometers, microcoil spectroscopy, and "NMR on a Chip" for chemistry, biochemistry, and industry, Chem. Rev. 114 (11) (2014) 5641–5694.
[2] J. Anders, P. SanGiorgio, X. Deligianni, et al., Integrated active tracking detector for MRI-guided interventions, Magn. Reson. Med. 67 (2012) 290–296.
[3] S. Sathyanarayana, P.A. Bottomley, MRI endoscopy using intrinsically localized probes, Med. Phys. 36 (2009) 908–919.
[4] C. Qian, G. Zabow, A. Koretsky, Engineering novel detectors and sensors for MRI, J. Magn. Reson. 229 (2013) 67–74.
[5] J.C. Ginefri, A. Rubin, M. Tatoulian, et al., Implanted, inductively-coupled, radiofrequency coils fabricated on flexible polymeric material: application to in vivo rat brain MRI at 7T, J. Magn. Reson. 224 (2012) 61–70.
[6] L. Renaud, M. Armenean, L. Berry, et al., Implantable planar rf microcoils for NMR microspectroscopy, Sens. Actuators A: Phys. 99 (2002) 244–248.
[7] M. Rata, V. Birlea, A. Murillo, et al., Endoluminal MR-guided ultrasonic applicator embedding cylindrical phased-array transducers and opposed-solenoid detection coil, Magn. Reson. Med. (2014), http://dx.doi.org/10.1002/mrm.25099.
[8] N.A. Volland, E.G. Kholmovski, D.L. Parker, et al., Initial feasibility testing of limited field of view magnetic resonance thermometry using a local cardiac radiofrequency coil, Magn. Reson. Med. 70 (2013) 994–1004.
[9] Y. Eryaman, Y. Öner, E. Atalar, Design of internal MRI coils using ultimate intrinsic SNR, Magn. Reson. Mater. Phys. Biol. Med. 22 (2009) 221–228.
[10] D. Hoult, P.C. Lauterbur, The sensitivity of the zeugmatographic experiment involving human samples, J. Magn. Reson. 34 (1979) 425–433.
[11] C. Massin, G. Boero, F. Vincent, et al., High-Q factor RF planar microcoils for micro-scale NMR spectroscopy, Sens. Actuators A: Phys. 97 (2002) 280–288.
[12] A.-L. Coutrot, E. Dufour-Gergam, J.-M. Quemper, et al., Copper micromoulding process for NMR microinductors realization, Sens. Actuators A: Phys. 99 (2002) 49–54.
[13] W. Wu, H. Yi, D. Chen, et al., The design and fabrication of a low-field NMR probe based on a multilayer planar microcoil, Microsyst. Technol. 20 (2014) 419–425.
[14] F. Herrault, S. Yorish, T.M. Crittenden, et al., Parylene-insulated ultradense microfabricated coils, J. Microelectromech. Syst. 19 (2010) 1277–1283.
[15] S. He, F. Chen, Q. Yang, et al., Facile fabrication of true three-dimensional microcoils inside fused silica by a femtosecond laser, J. Micromech. Microeng. 22 (2012) 105017.
[16] M. Couty, S. Nazeer, C. Jelita, et al., Ultra-flexible micro-antennas on PDMS substrate for MRI applications, in: Design, Test, Integration and Packaging of MEMS/MOEMS (DTIP), 2012 Symposium on, IEEE, 2012, pp. 126–131.
[17] B. Sarioglu, M. Tumer, U. Cindemir, et al., An optically powered CMOS tracking system for 3 T magnetic resonance environment, IEEE Trans. Biomed. Circuits Syst. (2014), http://dx.doi.org/10.1109/TBCAS.2014.2311474.
[18] R. Syms, I. Young, M. Ahmad, et al., Thin-film detector system for internal magnetic resonance imaging, Sens. Actuators A: Phys. 163 (2010) 15–24.
[19] R. Syms, I.R. Young, M.M. Ahmad, et al., Magneto-inductive catheter receiver for magnetic resonance imaging, IEEE Trans. Biomed. Eng. 60 (9) (2013) 2421–2431.
[20] C. Brace, Thermal tumor ablation in clinical use, Pulse IEEE 2 (2011) 28–38.
[21] V. Rieke, K. Butts Pauly, MR thermometry, J. Magn. Reson. Imaging 27 (2008) 376–390.
[22] M. Rata, R. Salomir, R. Umathum, et al., Endoluminal ultrasound applicator with an integrated RF coil for high-resolution magnetic resonance imaging-guided high-intensity contact ultrasound thermotherapy, Phys. Med. Biol. 53 (2008) 6549.
[23] I.P. Wharton, I.H. Rivens, G.R. Ter Haar, et al., Design and development of a prototype endocavitary probe for high-intensity focused ultrasound delivery with integrated magnetic resonance imaging, J. Magn. Reson. Imaging 25 (2007) 548–556.
[24] K. Segkoonthod, R. Syms, I. Young, Design of magneto-inductive magnetic resonance imaging catheters, IEEE Sens. J. 14 (5) (2013) 1505–1513.
[25] G.J. Stanisz, E.E. Odrobina, J. Pun, et al., T1, T2 relaxation and magnetization transfer in tissue at 3T, Magn. Reson. Med. 54 (2005) 507–512.
[26] C. Weidensteiner, N. Kerioui, B. Quesson, et al., Stability of real-time MR temperature mapping in healthy and diseased human liver, J. Magn. Reson. Imaging 19 (2004) 438–446.
[27] F. Hübner, B. Bazrafshan, J. Roland, et al., The influence of Nd:YAG laser irradiation on Fluoroptic® temperature measurement: an experimental evaluation, Lasers Med. Sci. (2013) 1–10.
[28] T.E. Conturo, G.D. Smith, Signal-to-noise in phase angle reconstruction: dynamic range extension using phase reference offsets, Magn. Reson. Med. 15 (1990) 420–437.
[29] R.D. Peters, R.M. Henkelman, Proton-resonance frequency shift MR thermometry is affected by changes in the electrical conductivity of tissue, Magn. Reson. Med. 43 (2000) 62–71.
[30] M.N. Streicher, A. Schäfer, E. Reimer, et al., Effects of air susceptibility on proton resonance frequency MR thermometry, Magn. Reson. Mater. Phys. Biol. Med. 25 (2012) 41–47.
[31] I.R. Young, J.V. Hajnal, I.G. Roberts, et al., An evaluation of the effects of susceptibility changes on the water chemical shift method of temperature measurement in human peripheral muscle, Magn. Reson. Med. 36 (1996) 366–374.

Biographies

Evdokia M. Kardoulaki received the Ph.D. degree in CMOS hyperbolic sine filter design for low/audio frequency biomedical applications from the Department of Bioengineering, Imperial College London, U.K., in 2012. She is currently a post-doctoral researcher in Electrical and Electronic Engineering Department, Imperial College London. Her research interests include circuits and sensors for biomedical applications, medical imaging, MR-thermometry and MR-safety.

Richard R. A. Syms is a Professor of microsystems technology from the Electrical and Electronic Engineering Department, Imperial College London, London, U.K., where he heads the Optical and Semiconductor Devices Group. He has published over 200 journal and conference papers on electromagnetic theory, sensors, meta-materials, and medical imaging. He is a Fellow of the Royal Academy of Engineering, the Institute of Electrical Engineers, and the Institute of Physics.

Ian R. Young is a Senior Research Fellow with the Electrical and Electronic Engineering Department, Imperial College London, U.K. He has published over 300 papers on MRI. His current interests are in vivo MRI and MR-guided surgical robots. He is a Fellow of the Royal Society and the Royal Academy of Engineering, and he received the Gold Medal of SMRM and the Sir Frank Whittle Prize.

Marc Rea received the Ph.D. degree in MR-compatible systems for prostate biopsy from Imperial College London, London, U.K., in 2010. He is currently a Clinical Scientist at St. Mary's Hospital, London. His research interests include medical robotics, MRI-compatible device tracking, and high-intensity focused ultrasound.

Wladyslaw M.W. Gedroyc has been a full-time radiology consultant at St Mary's Hospital in London (Imperial College healthcare NHS trust) since 1990. He holds a chair in radiology at Imperial College London and has been involved with MR-guided focused ultrasound work for the last 12 years. He is also a pioneer in other MR-guided interventional techniques. He has authored more than 105 peer-reviewed papers and is the principal investigator on multiple grants in this field.